

Acoustic imaging by three-dimensional acoustic Luneburg meta-lens with lattice columns

Jung-Woo Kim,¹ Seong-Jin Lee,² Jun-Yeong Jo,² Semyung Wang,¹ and Sang-Hoon Kim^{2, a)}

¹*School of Mechanical Engineering, Gwangju Institute of Science and Technology, 123 Cheomdangwagi-ro, Buk-gu, Gwangju 61005, Republic of Korea*

²*Division of Marine Engineering, Mokpo National Maritime University, 91 Haeyangdaehak-ro, Mokpo 58628, Republic of Korea*

(Dated: 26 November 2020)

A three-dimensional acoustic Luneburg lens, or acoustic Luneburg ball, has the advantage of refracting sound waves for all incident angles and concentrating higher sound pressure compared to a two-dimensional lens. A lens with a radius of 60 mm was designed with thousands of unit atoms comprising lattice columns to maintain its shape. The focusing performance of the lens was simulated using COMSOL Multiphysics, a finite element analysis program. Acoustic imaging was performed at a frequency of 10 kHz using a microphone, transducer, three-axis linear stage, and LabVIEW-based measurement program for a plastic lens made by a selective laser sintering 3D printer. The omnidirectional property was confirmed by measuring the sound pressure level while rotating the lens. The sound pressure level gain was defined to represent the frequency-dependent performance of the lens, and the maximum values were measured at approximately 20 dB and 15 dB in the numerical simulation and the experiment, respectively, at a frequency of 16 kHz. The results suggest that acoustic meta-lenses can be used for acoustic communication, imaging systems, and energy harvesting.

Keywords: Luneburg lens, gradient index lens, meta-lens, metamaterial, acoustic imaging

The Luneburg lens was proposed by Luneburg in the 1940s as a typical model of the wave transformation theory,¹ and studied in the context of geometrical optics by Gutman in the 1950s.² The general solution of the lens was presented by Morgan,³ and Boyles studied the properties of the lens and concluded that it was important to establish the density conditions for an acoustic Luneburg lens with perfect focusing properties at certain frequencies.^{4,5} Applying these gradient-index (GRIN) lens methods, the two-dimensional (2D) Luneburg lens was optically realized through numerical simulation, fabrication, and experimentation.⁶⁻⁹ Zentgraf et al. realized a plasmonic Luneburg lens capable of focusing surface plasmon polaritons using grayscale lithography.¹⁰ These studies have been extended to the three-dimensional (3D) Luneburg lenses. Ma et al. reported a numerical simulation and experimental results for the lens radiation pattern by designing a 3D lens with a wide frequency band of 12.4-18 GHz using quasi-conformal mapping.¹¹ Zhao et al. demonstrated the focusing performance of a 3D lens designed with cubic metamaterial structures in the microwave domain.¹² These types of lenses have also been applied as superlenses to overcome the diffraction limit.¹³

In addition, many studies have been performed on the Luneburg meta-lens, which is acoustically realized and applicable to a wide range of frequencies. Studies on phononic crystals (PCs), band gaps, etc.,^{14,15} as well as sound-focusing studies on acoustic GRIN lenses, have been conducted based on these studies.¹⁶⁻²¹ Kim initially realized a 2D acoustic Luneburg lens with a metastructure to verify its performance in the audible frequency range.²² Dong et al. demonstrated that a 2D flattened acoustic Luneburg lens designed using

a quasi-conformal mapping operates at a frequency of 3-7 kHz.²³ Zhu et al. demonstrated anisotropic acoustic metamaterials by combining a Luneburg lens and a fisheye lens.²⁴ Park et al. successfully implemented the aberration-free property of a lens composed of orifice-type unit cells.²⁵ Fu et al. demonstrated that the lens could be used as a retroreflector.²⁶ In addition, an underwater 2D flat lens was studied.^{27,28} Recently, research on acoustic meta-lenses has expanded from 2D to 3D, because 3D lenses have the advantage of focusing incident waves at all angles compared to the 2D lenses. They can also achieve a higher sound pressure level (SPL) than the 2D lenses, and have an omnidirectional property with the same focusing performance for incident waves in all directions. Xie et al. fabricated a 2D and a 3D lens and measured the performance of the 2D lens in the ultrasound frequency range.²⁹ Zhao et al. reported ultrasonic beam steering based on 2D and 3D flattened lenses at 40 kHz.³⁰ They successfully demonstrated beam steering from 0° to 45° by a 3D lens in the air. Allam et al. studied the focusing performance of an underwater GRIN PC lens.³¹ Despite these pioneering studies, the acoustic imaging of 3D acoustic Luneburg lenses with frequency-dependent acoustic focusing properties has not been reported.

In this paper, we report the design method, numerical simulation, and measurement results of an acoustic Luneburg ball in air. We confirmed the agreement between numerical simulations and measurement results, and demonstrate the focusing performance of the ball through its omnidirectional property, SPL gain, and acoustic imaging.

The method to design a Luneburg ball is as follows. If the difference in acoustic impedance between the medium and the lattice column is too large, the sound wave does not pass through the structure. That is, the wave does not pass through the unit atoms constituting the lens, but passes between the unit cells and unit atoms. A polyamide, which has a specific

^{a)}Electronic mail: shkim@mmu.ac.kr, Corresponding author

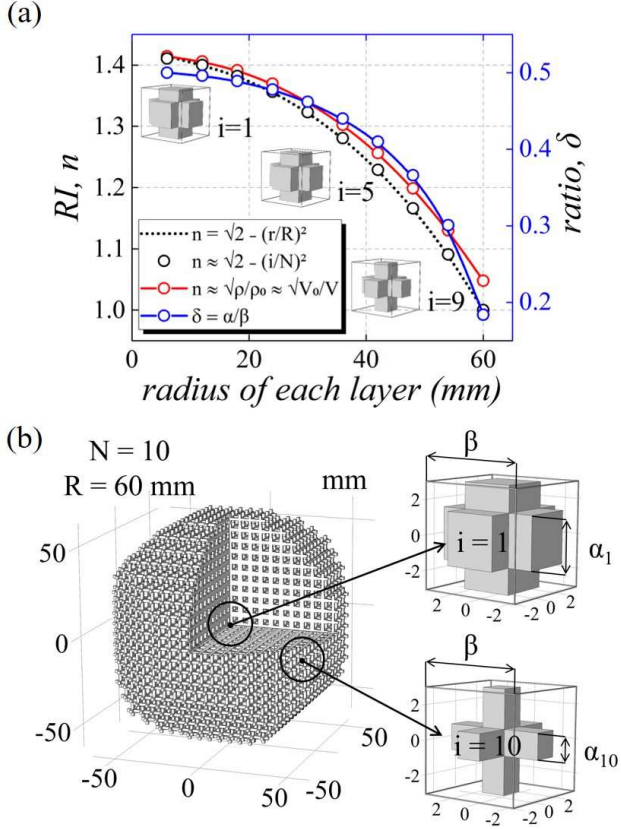


FIG. 1. (a) The refractive index (RI, n) and the ratio ($\delta = \alpha/\beta$) according to the radius of each layer. (b) The design and modeling of the Luneburg ball and its lattice columns.

acoustic impedance $Z = \rho c$ ($\rho \approx 1,000 \text{ kg/m}^3$, $c \approx 2,200 \text{ m/s}$, $Z \approx 2,200 \text{ krayls}$) and can be fabricated by a selective-laser-sintering (SLS) 3D printer, is selected. The Z value of the material is approximately 5,000 times larger than that of air ($\rho \approx 1.225 \text{ kg/m}^3$, $c \approx 343 \text{ m/s}$, $Z \approx 0.420 \text{ krayls}$). Therefore, the wave path is established as the space between the unit cells and unit atoms. The refractive index (RI, n) of the sound wave is $n = \sqrt{\rho_r \kappa_r}$, where ρ_r is the relative density and κ_r is the relative compressibility of the medium. If the medium does not change while the sound wave passes, then the compressibility is almost constant. Therefore, the RI is determined only by the density of the space through which the wave passes ($n \propto \sqrt{\rho_r}$). The RI is obtained from the relative density as $n = v_0/v \approx \sqrt{\rho/\rho_0} \approx \sqrt{V_0/V}$, where v_0 , ρ_0 , V_0 are the background velocity, density, and volume. On the other hand, v , ρ , V are the properties of the medium when there are obstacles with a large acoustic impedance.

In the design of the 3D lens, the unit atoms were designed as lattice columns. α_i and β are the dimensions of the obstacles and unit atoms in FIG. 1. The radius of the lens is $R = 60$ mm, and the length of a cubic unit cell is $\beta = 6$ mm. α_i is the length of one side of the i^{th} unit atoms and varies depending on the position of the layers. Because the previously derived RI-volume relation is derived as $n \approx \sqrt{V_0/V} \approx$

$\sqrt{\beta^3/\beta^3 - (3\beta\alpha_i^2 - 2\alpha_i^3)}$ when expressed in α_i and β . If the ratio of the length of one side of the unit atoms and that of the unit cells is 0, the unit atom does not exist; if it is equal to 1, the wave does not pass because the unit atom fills the unit cell; and if it is greater than 1, the unit atom exceeds the size of the unit cell. Therefore, the ratio is set to $0 < \delta(i) = \alpha_i/\beta < 1$, then the refractive index is $n(i) = 1/\sqrt{1 - 3\delta(i)^2 + 2\delta(i)^3}$.

The Luneburg lens RI formula is

$$n = \sqrt{2 - (r/R)^2} \quad (1)$$

where R is the radius of the lens and r is the distance from the center of the lens. As a function of the radius, the RI has a maximum value of $\sqrt{2}$ at the center, and decreases toward the outside to 1, equal to the RI of the medium. Therefore, it is defined as a GRIN lens that can focus the incident wave without aberration, as shown in Eq. (1). Because it is spherically symmetric, it is possible to discretize the volume as many concentric layers. If the lens is divided into N layers, the RI is newly defined as $n \approx \sqrt{2 - (i/N)^2}$ ($= \sqrt{2 - (r/R)^2}$), where $i = 0, 1, 2, \dots, (N-1)$, and $N = 10$ ($= R/\beta$) is chosen in the design. As a result, the RI-volume relation and the Luneburg lens RI formula in the case of discretizing into N are the same, so the formula for designing the lens is as follows.

$$\frac{2 - (i/N)^2}{2\delta^3 - 3\delta^2 + 1} = 1 \quad (2)$$

The dimensions of the unit atoms constituting each layer can be obtained from Eq. (2). The similarity between each RI and the ratio δ can be confirmed by the comparison in FIG. 1(a). The design and modeling results of the Luneburg ball are shown in FIG. 1(b). The sizes of the lattice columns increase toward the center of the lens, the RI changes for each layer, and the speed of the incident sound wave decreases, so that the sound wave that passes through the lens can be concentrated on the opposite side without aberration.

To compare the designed lens with an ideal lens, a numerical simulation of the designed model and the formula model that applies the Luneburg lens RI formula to a 60 mm sphere is performed using COMSOL Multiphysics, and the plane wave propagates from the right to the left of the lens, as shown in FIG. 2 ((FIG. 2(a) is an enlarged view of FIG. 2(c)). The method sets the medium of the cuboid area (360 mm x 130 mm x 130 mm) to air and places the lens at the center. To eliminate the reflection of sound waves, the surrounding area is set to a 30 mm thick perfectly matched layer (PML). In particular, to shorten the analysis time and cost, the simulation is carried out with the entire geometry cut by 1/4. The formula model can refract the waves more gradually than the designed model, so the designed model has a slightly longer focusing distance compared to the formula model. The sound waves are concentrated well from 5 to 15 kHz, but not at 20 kHz, as shown in FIGs. 2 (c)-(f). Thus, we can see that a focusing frequency range exists, depending on its geometry. The unit atoms have a subwavelength size that is smaller than the wavelength at which the lens interacts, and must be smaller

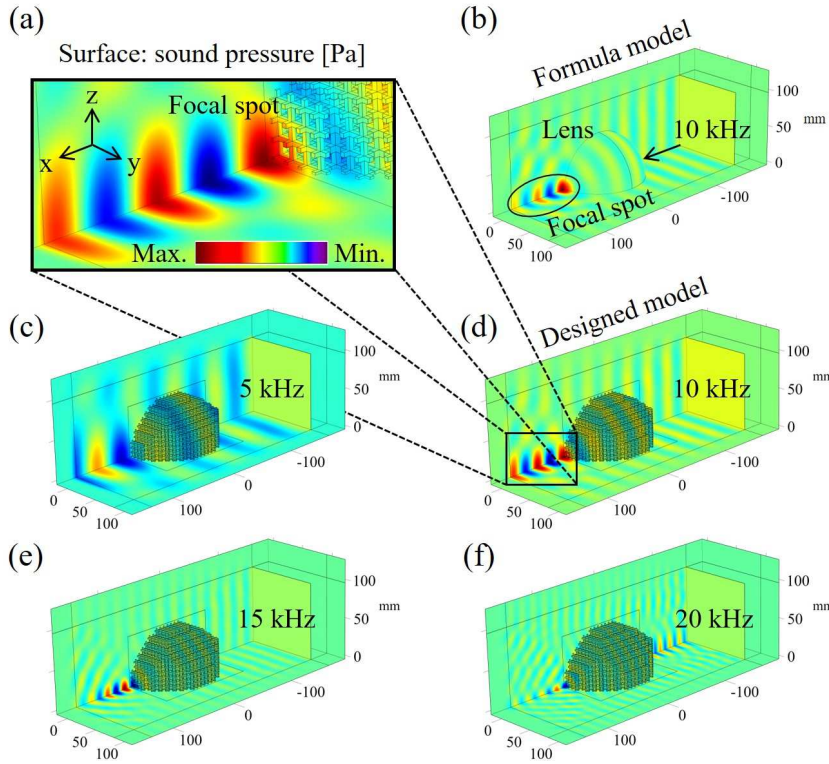


FIG. 2. Frequency-dependent focusing performance by the numerical simulation of the formula and designed model. (a) Enlarged view of the focusing area in (d). (b) Formula model at 10 kHz. (c) Designed model at 5 kHz, (d) 10 kHz, (e) 15 kHz, and (f) 20 kHz.

than the diameter of the lens to diffract the wave. In addition, the applicable frequency range depends on the RI and acoustic impedance.

After confirming the focusing performance by the numerical simulation, a polyamide lens was fabricated using a SLS 3D printer. The experimental setup for the placement of the lens, transducer, and microphone is shown in FIG. 3(a). A supporter was designed under the lens, which was completely fixed to a plastic structure. When sound waves were propagated from the transducer to the Luneburg ball in air, the microphone measured the sound pressure level around the lens. The schematic diagram in FIG. 3(b) explains the connections between the measuring equipment and the process of measuring the performance of the lens. We used an amplifier (B&K 2692-A), oscilloscope, function generator, three-axis linear stage, and a LabVIEW-based measurement program to process the signal obtained by sending a signal from a transducer and moving a microphone (B&K 4138-A-015) around the lens. Acoustic pulse signals were generated by the transducer, which had a signal amplitude of 2 V, burst count of 25, burst period of 50 ms, and wait time of 500 ms.

The measurement methods were largely divided into three parts. Before signals were passed through the lens, 5 mm was set as the input section, and the average SPL was calculated. In addition, the maximum value of SPL was calculated by setting the area passing through the lens as an output section 70 mm. Defining and calculating the SPL gain (= output - input), we attempted to express the focusing performance of the lens by frequency as a value. The next stage was to measure the SPL by rotating the lens (10°, 20°, 30°, and 40°), which demonstrated the performance according to the incident direc-

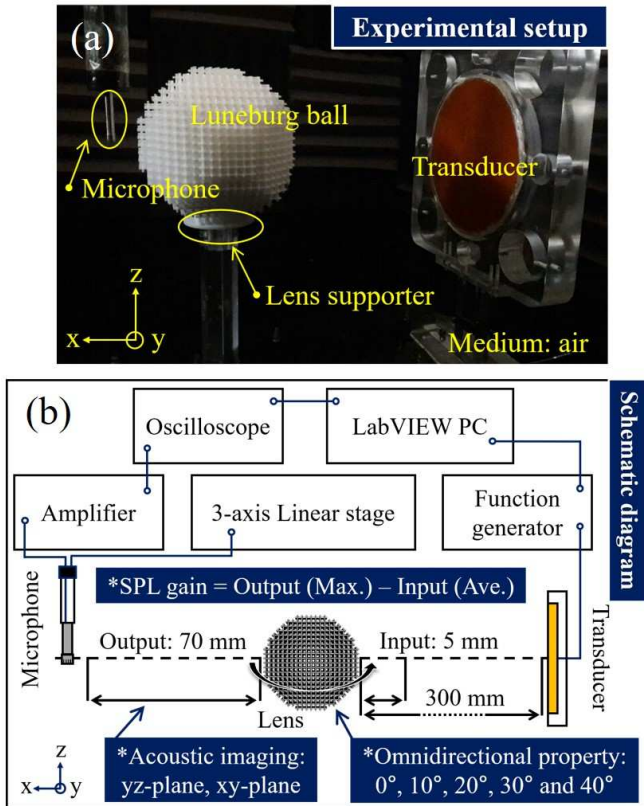


FIG. 3. (a) Experimental setup. (b) Schematic diagram of the measurement.

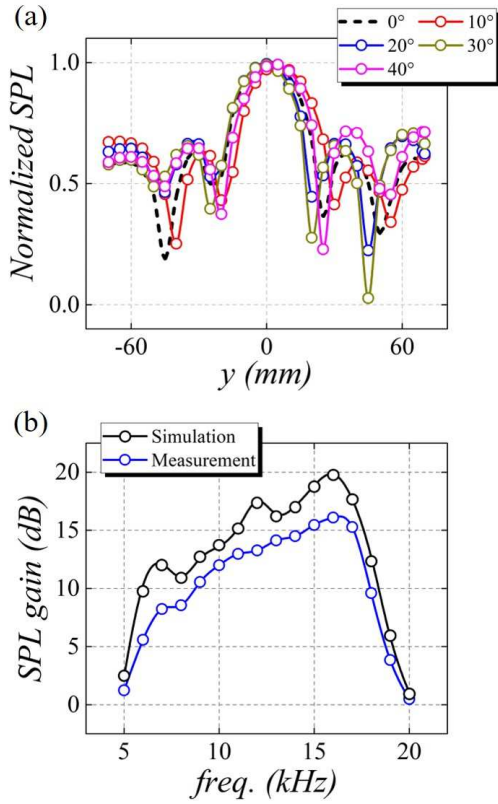


FIG. 4. (a) Normalized focusing performance depending on the incident angles (0° , 10° , 20° , 30° , and 40°) expressed as normalized SPLs. (b) Comparison of frequency-dependent SPL gain.

tion without moving the transducer. Because the lens is spherically symmetric, it should exhibit the same performance in all directions in principle. Finally, the acoustic imaging was measured by the y-z plane (140 mm x 140 mm) and x-y plane (70 mm x 140 mm) regions by 1 mm.

The omnidirectional property is shown in Fig. 4(a). The normalized SPL on the y-axis by setting different incident directions was recorded. The spherical symmetry of the lens can be confirmed through the same tendency and focusing performance. The maximum SPL gain was approximately 20 dB at 16 kHz in the simulation, but the measured result was approximately 15 dB, as shown in Fig. 4(b). The reason for the difference in SPL gain is that it is difficult to realize the designed model without error when fabricating the lens with an SLS 3D printer. In addition, the reflection of sound waves was minimized through PML during the simulation, but these effects cannot be completely eliminated when measured in practice. The normalized SPLs for the y-z plane and x-y plane were plotted in the 3D space, as shown in FIGs. 5(a) and (b). In the y-z plane, it can be confirmed by acoustic imaging that the highest SPL is measured near the center of the lens. In the x-y plane, the highest SPL can be seen in front of the lens, and it decreases as the distance increases. Comparison between numerical simulation and measurement results in the two directions is shown in FIGs. 5(c) and (d). We see that the trends are similar, and there is a very little difference between

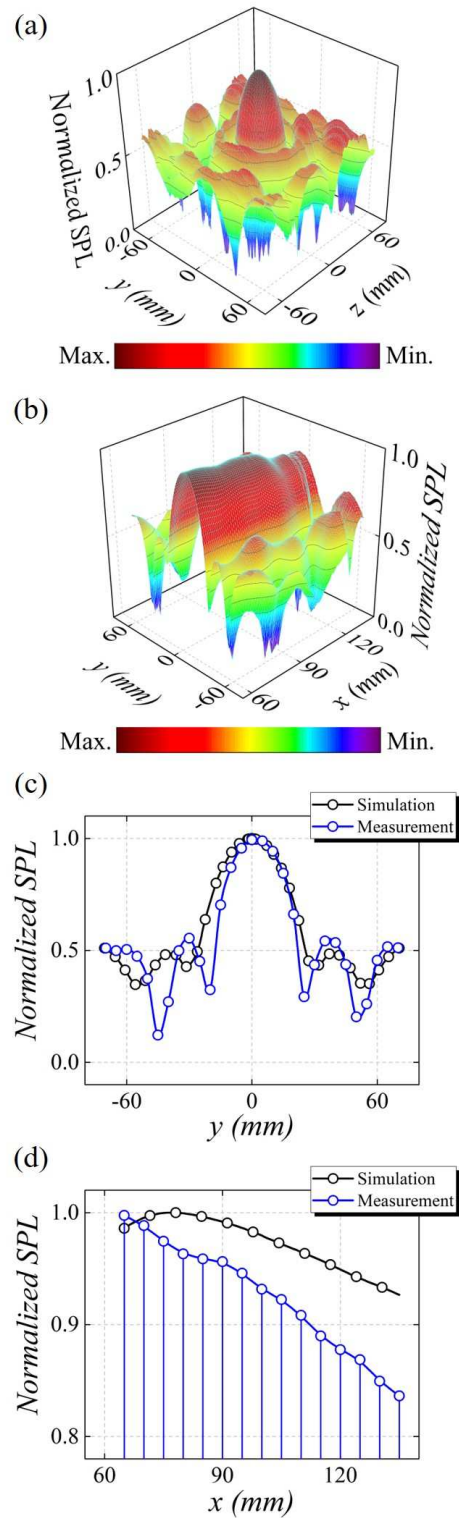


FIG. 5. (a) and (b) are 3D surfaces of the acoustic imaging in the y-z plane and x-y planes, respectively, expressed as normalized SPL. (c) and (d) are graphs of the focusing performance compared to the numerical simulation and measurement results on the y-axis and x-axis, respectively, expressed as normalized SPLs.

the normalized SPL values, indicating that the lens design,

fabrication, and measurement process were successfully performed.

We designed, simulated, fabricated, and measured a 3D acoustic Luneburg lens (or acoustic Luneburg ball) beyond the scope of 2D lenses. Using the RI formula, the unit atoms were designed as lattice columns to realize a 3D lens discretized into ten layers. Before fabricating the Luneburg ball, its focusing performance was verified through numerical simulation. The 3D lens has spherical symmetry, and its omnidirectional property was verified by measuring the SPL while rotating the lens. Because the performance of the lens is frequency-dependent, the SPL gain was defined and measured, and as a result, an applicable frequency range of approximately 5 to 17 kHz was confirmed. The maximum SPL gain was measured at approximately 20 dB and 15 dB in the numerical simulation and the experiment, respectively, at a frequency of 16 kHz. The acoustic imaging of the ball was measured in the y-z and x-y planes at a frequency of 10 kHz. These results suggest that the acoustic meta-lenses can be used for acoustic communication, imaging systems, and energy harvesting. Specifically, they could be applied in non-destructive testing or ultrasonography to improving imaging performance, and owing to their omnidirectional property, a complex phase-shift network is not required, so they can be used to develop next-generation sonar for underwater communication.³²⁻³⁴

ACKNOWLEDGEMENTS

This work was supported by the 2019 Undergraduate Research Program of the Korean Foundation for the Advancement of Science & Creativity. This work was supported by GIST Research Institute(GRI) grant funded by the GIST in 2020.

DATA AVAILABILITY

The data that support the findings of this study are available from the corresponding author upon reasonable request.

REFERENCES

- ¹R. K. Luneburg and M. Herzberger, *Mathematical Theory of Optics*, (University of California Press, Berkeley, Los Angeles, 1964).
- ²A. S. Gutman, *J. Appl. Phys.* **25**, 855 (1954).
- ³S. P. Morgan, *J. Appl. Phys.* **29**, 1358 (1958).
- ⁴C. A. Boyles, *J. Acoust. Soc. Am.* **45**, 351 (1969).
- ⁵C. A. Boyles, *J. Acoust. Soc. Am.* **45**, 356 (1969).
- ⁶Q. Cheng, H. F. Ma, and T. J. Cui, *Appl. Phys. Lett.* **95**, 181901 (2009).
- ⁷A. D. Falco, S. C. Kehr, and U. Leonhardt, *J. Opt. Soc. Am.* **19**, 5156 (2011).
- ⁸L. Zigoneanu, B.-I. Popa, and S. A. Cummer, *Phys. Rev. B* **84**, 024305 (2011).
- ⁹J. A. Dockrey, M. J. Lockyear, S. J. Berry, S. A. R. Horsley, J. R. Sambles, and A. P. Hibbins, *Phys. Rev. B* **87**, 125137 (2013).
- ¹⁰T. Zentgraf, Y. Liu, M. H. Mikkelsen, J. Valentine, and X. Zhang, *Nat. Nanotechnol.* **6**, 151 (2011).
- ¹¹H. F. Ma and T. J. Cui, *Nat. Commun.* **1**, 124 (2010).
- ¹²Y.-Y. Zhao, Y.-L. Zhang, M.-L. Zheng, X.-Z. Dong, X.-M. Duan, and Z.-S. Zhao, *Laser Photonics Rev.* **10**, 665 (2016).
- ¹³X. Zhang and Z. Liu, *Nat. Mater.* **7**, 435 (2008).
- ¹⁴M. S. Kushwaha, P. Halevi, L. Dobrzynski, and B. Djafari-Rouhani, *Phys. Rev. Lett.* **71**, 2022 (1993).
- ¹⁵M. Sigalas and E. N. Economou, *Solid State Commun.* **86**, 141 (1993).
- ¹⁶S. Yang, J. H. Page, Z. Liu, M. L. Cowan, C. T. Chan, and P. Sheng, *Phys. Rev. Lett.* **93**, 024301 (2004).
- ¹⁷M. Ke, Z. Liu, Z. Cheng, J. Li, P. Peng, and J. Shi, *Solid State Commun.* **142**, 177 (2007).
- ¹⁸S.-C. S. Lin, T. J. Huang, J.-H. Sun, and T.-T. Wu, *Phys. Rev. B* **79**, 094302 (2009).
- ¹⁹A. Climente, D. Torrent, and J. Sánchez-Dehesa, *Appl. Phys. Lett.* **97**, 104103 (2010).
- ²⁰D. Torrent, Y. Pennec, and B. Djafari-Rouhani, *J. Appl. Phys.* **116**, 224902 (2014).
- ²¹H. S. Kang and K. I. Lee, *New Phys.: Sae Mulli* **69**, 673 (2019).
- ²²S.-H. Kim, in *2014 8th International Congress on Advanced Electromagnetic Materials in Microwaves and Optics (METAMATERIALS)* (IEEE, 2014).
- ²³H. Y. Dong, Q. Cheng, G. Y. Song, W. X. Tang, J. Wang, and T. J. Cui, *Appl. Phys. Express* **10**, 087202 (2017).
- ²⁴R. Zhu, C. Ma, B. Zheng, M. Y. Musa, L. Jing, Y. Yang, H. Wang, S. Dehdashti, N. X. Fang, and H. Chen, *Appl. Phys. Lett.* **110**, 113503 (2017).
- ²⁵C. M. Park and S. H. Lee, *Appl. Phys. Lett.* **112**, 074101 (2018).
- ²⁶Y. Fu, J. Li, Y. Xie, C. Shen, Y. Xu, H. Chen, and S. A. Cummer, *Phys. Rev. Mater.* **2**, 105202 (2018).
- ²⁷X. Su, A. N. Norris, C. W. Cushing, M. R. Haberman, and P. S. Wilson, *J. Acoust. Soc. Am.* **141**, 4408 (2017).
- ²⁸H. Sun, S. Wang, S. Huang, L. Peng, Q. Wang, and W. Zhao, *Sci. Rep.* **10**, 1469 (2020).
- ²⁹Y. Xie, Y. Fu, Z. Jia, J. Li, C. Shen, Y. Xu, H. Chen, and S. A. Cummer, *Sci. Rep.* **8**, 16188 (2018).
- ³⁰L. Zhao, E. Laredo, O. Ryan, A. Yazdkhasti, H.-T. Kim, R. Ganye, T. Horriuchi, and M. Yu, *Sci. Rep.* **116**, 071902 (2020).
- ³¹A. Allam, K. Sabra, and A. Erturk, *Phys. Rev. Appl.* **13**, 064064 (2020).
- ³²Y. Chen, H. Liu, M. Reilly, H. Bae, and M. Yu, *Nat. Commun.* **5**, 5247 (2014).
- ³³Y. Jin, R. Kumar, O. Poncelet, O. Mondain-Monval, and T. Brunet, *Nat. Commun.* **10**, 143 (2019).
- ³⁴S.-H. Kim, B.-W. Ahn, K.-M. Park, and G.-S. Lim, e-print arXiv:1906.07174 (2019).